Remote sensing of cirrus cloud optical thickness and effective particle size for the National Polar-orbiting Operational Environmental Satellite System Visible/Infrared Imager Radiometer Suite: sensitivity to instrument noise and uncertainties in environmental parameters

Szu-Cheng Ou, Yoshihide Takano, K. N. Liou, Glenn J. Higgins, Adrian George, and Richard Slonaker

We describe sensitivity studies on the remote sensing of cirrus cloud optical thickness and effective particle size using the National Polar-orbiting Operational Environmental Satellite System Visible/Infrared Imager Radiometer Suite 0.67-, 1.24-, 1.61-, and 2.25-μm reflectances and thermal IR 3.70- and 10.76-μm radiances. To investigate the accuracy and precision of the solar and IR retrieval methods subject to instrument noise and uncertainties in environmental parameters, we carried out signal-to-noise ratio tests as well as the error budget study, where we used the University of California at Los Angeles line-by-line equivalent radiative transfer model to generate radiance tables for synthetic retrievals. The methodology and results of these error analyses are discussed. © 2003 Optical Society of America

OCIS codes: 280.0280, 120.0280.

1. Introduction

The importance of cirrus clouds in weather and climate processes has been recognized as a result of numerous observational and modeling studies. Information on cirrus cloud parameters is critically important to the development of cloud forecast models, the upgrading of real-time global cloud analyses, the investigation of cloud feedbacks in the global climate change study, and the development of algorithms for the remote sensing of aerosols and surface parameters. In response to this need, routine and operational methods for the satellite remote sensing of cirrus cloud optical thickness (COT) and effective particle size (EPS) have been implemented in the moderate-resolution imaging spectroradiometer (MODIS) and Clouds and the Earth's Radiant Energy System (CERES) cloud retrieval packages.[1,2] These methods assume plane-parallel geometry for the modeling of atmospheric radiative transfer, and they exploit characteristics of radiometric band wavelengths at which absorption by water vapor and other gases is minimal and at which the scattering and absorption by cloud particles are sensitive to the ice crystal size distribution. In general, satellite cirrus cloud remote sensing techniques can be divided into those that use solar reflectance and those that use emitted thermal infrared (IR) radiance.[3]

The development of techniques that use solar reflectance started from a number of studies on the determination of COT and effective particle radius by use of measured reflectance from airborne visible and near-IR radiometers.[4–6] These techniques are

S.-C. Ou (ssou@atmos.ucla.edu), Y. Takano, and K. N. Liou are with the Department of Atmospheric Sciences, University of California, Los Angeles, Los Angeles, California 90095-1565. G. J. Higgins is with Northrop Grumman TASC, Chantilly, Virginia 20151-3822. A. George is with the Lincoln Laboratory, Massachusetts Institute of Technology, Lexington, Massachusetts 02420-9185. R. Slonaker is with the Raytheon ITSS Corporation, Lanham, Maryland 20706-4932.

Received 24 February 2003; revised manuscript received 10 July 2003.

0003-6935/03/367202-13$15.00/0

based on the principle that the reflection function of clouds at a nonabsorbing channel for water and ice particles in the visible spectral region is primarily a function of the COT, whereas the reflection function at an absorbing channel in the short-wave IR (e.g., 1.61- and 2.25-μm channels) is primarily a function of the cloud particle size.[7,8] Previous studies have demonstrated that remote sensing methods with visible and short-wave IR channel reflectances can be applied to the determination of optical and microphysical properties of water clouds. The determination of cirrus cloud microphysical and optical properties by use of the same principle of correlation between the MODIS Airborne Simulator 0.657- and 1.609-μm channel reflectances has been successfully demonstrated.[9,10]

In the past, cirrus cloud parameters have also been inferred by use of thermal IR imaging and sounding channels.[11–13] In particular, Ou *et al.*[14] developed a physical retrieval scheme using the advanced very high resolution radiometer (AVHRR) 3.7- and 10.9-μm channel radiances to infer nighttime cirrus cloud parameters, including cloud temperature, optical thickness, and mean effective ice crystal size, based on the theory of radiative transfer and parameterizations. This retrieval scheme has been applied to the nighttime AVHRR data collected during the First International Satellite Cloud Climatology Project Regional Experiment (FIRE-I) Phase I, intensive field observation. To apply this IR retrieval scheme to local daytime scenes, a numerical approach used to remove the solar component in the 3.7-μm radiance has been incorporated into the algorithm.[15] The resulting removal–retrieval program was tested with AVHRR data collected during both FIRE-I and FIRE-II intensive field observations over respective observation sites.[16] Validation of the cirrus cloud parameters generated by this program has been carried out with collocated aircraft and balloonborne *in situ* ice crystal size distribution from two-dimensional probe measurements and ground-based lidar return imageries.[15–17]

The research presented here was executed to assist the design for the National Polar-orbiting Operational Environmental Satellite System's (NPOESS) Visible/Infrared Imager/Radiometer Suite (VIIRS). The VIIRS is being developed as part of the NPOESS platform to satisfy the operational requirements for the global remote sensing of atmospheric and surface properties. One of the prime applications of VIIRS channels is the remote sensing of cloud properties, including optical thickness, particle size, cloud-top temperature, cloud cover and cloud layers, and cloud height. These parameters are generally termed cloud environmental data records (EDRs). Here, we address the two NPOESS cloud EDRs: the COT and the EPS. We assume a single layer of cirrus cloud. The principle of the solar two-channel correlation technique and the IR two-channel retrieval method is now applied to the development of VIIRS solar and IR schemes for both nighttime and daytime conditions. Although initial success has been achieved for the retrieval of cloud optical and microphysical parameters by these two approaches that were applied to surrogate satellite and airborne data, further algorithm sensitivity and validation studies are required to assess the accuracy and precision of these methods when applied to global cirrus cloud mapping with the VIIRS instrument. In the remainder of this paper we use cloud optical depth as an alternative terminology to denote the COT.

In Section 2 we present instrument characteristics and the theoretical basis for the cirrus cloud solar and IR retrieval algorithms. We briefly describe the structure of the University of California at Los Angeles (UCLA) line-by-line equivalent (LBLE) radiative transfer program that has been developed specifically to simulate the clear and cloudy reflectance and radiance to facilitate the development of and sensitivity analyses for cloud retrieval approaches with the VIIRS radiometer. The retrieval methods to infer COT and EPS, together with the prospective VIIRS radiometer, are being developed to satisfy the specifications in the NPOESS Sensor Requirements Document (SRD)[18] for the respective cloud EDRs. Under the VIIRS radiometer development concept, these specifications flow down to the most cost-effective design solution that satisfies the SRD requirements. To investigate the accuracy and precision of the retrieval methods subject to instrument noise and uncertainties in environmental parameters, we carried out a series of signal-to-noise ratio (SNR) tests and error budget analyses, which effectively simulate radiometer and retrieval performance for several environmental and operational cases. With these tests and analyses we investigate the synthetic retrieval accuracy and precision using the SRD's threshold and objective requirements as references. The threshold is the largest error allowable for a retrieval method, and the objective is the optimal error limit that a retrieval method should strive to achieve. Comprehensive studies have been performed under the support of Raytheon ITSS and have been described in detail in Ou *et al.*[19] Major results of SNR tests and error budget studies are described in Section 3. Finally, a summary is given in Section 4.

2. Description of Retrieval Methods

A. Instrument Characteristics

Figure 1 shows the wavelength locations of seven VIIRS visible and near-IR channels to be used for the retrieval of cloud optical depth and EPS. The atmospheric zenith transmittances from altitudes of 10, 5, and 0 km to the top of atmosphere are calculated from the LBLE model based on the U.S. Standard Atmosphere. The solar zenith angle is 32°. Note that all these channels, except the one at 1.378 μm, are located at window wavelengths associated with high atmospheric transmittance. At present, VIIRS is designed to scan through nadir in a cross-track plane perpendicular to the orbital ground track with the maximum viewing angle extending up to 56° on ei-

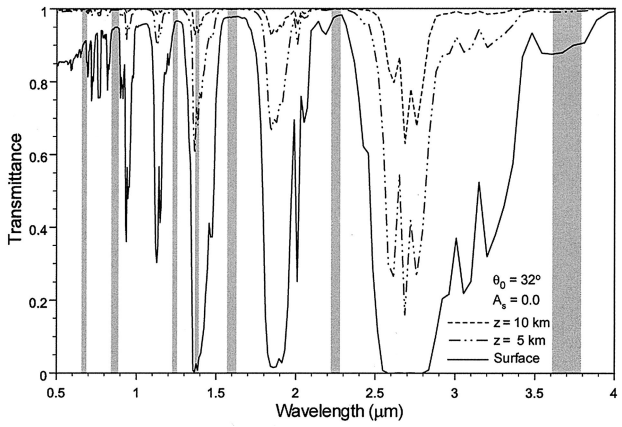

Fig. 1. Spectral characteristics of the seven VIIRS solar channels, centered at 0.67, 0.86, 1.24, 1.38, 1.61, 2.25, and 3.70 μm, used for retrievals of COT and EPS. The atmospheric zenith transmittances are calculated by the LBLE radiative transfer model for the atmospheric vertical range from altitudes of 10 km, 5 km, and surface to the top of atmosphere based on the U.S. Standard Atmosphere at 32° solar zenith angle.

ther side. At a nominal orbital altitude for the NPOESS platform of approximately 833 km, this yields a swath width of 3000 km centered on the satellite nadir orbital ground track. VIIRS is nominally composed of 16 radiometric channels. The cirrus cloud solar retrieval algorithm will use one visible channel (0.67 μm) and three short-wave IR channels (1.24, 1.61, and 2.25 μm). The IR algorithm will use one near-IR channel (3.70 μm) and one thermal IR channel (10.76 μm).

B. Definition of Ice Crystal Effective Particle Size

The development of remote sensing algorithms for ubiquitous cirrus clouds requires comprehensive knowledge of two fundamental ice microphysics parameters: ice crystal size distribution and ice crystal shape (habit). Both parameters vary in space and time and are associated with several complicated microphysical processes. For satellite remote sensing applications, it is necessary to define representative ice crystal size distributions and shapes for the calculation of phase functions and other relevant single-scattering properties. In conjunction with our ongoing radiative transfer and satellite remote sensing studies involving clouds, we analyzed six composite ice crystal size distributions that were obtained from aircraft observations over mid-latitude regions presented by Heymsfield and Platt,[20] Takano and Liou,[21,22] and the FIRE intensive field observation microphysical data archive. They are denoted as cold cirrus (Cold Ci), Ci($T = -60$ °C), cirrostratus (Cs), Ci (Nov. 1), Ci (Nov. 2), and Ci Uncinus; these ice crystal size distributions are shown in Ou *et al.*[19] The ice crystal sizes span from approximately 5 to 2000 μm with shapes ranging from bullet rosettes, solid and hollow columns, and plates to aggregates. It is possible to perform similar analyses on tropical cirrus cloud microphysical data. However, to produce representative ice crystal size distribution for tropical conditions, we need to have a more comprehensive data collection than is currently available.

We define the ice crystal EPS to characterize ice crystal size distribution in the form

$$D_e = \int D^2 L n(L) \mathrm{d}L \Big/ \int D L n(L) \mathrm{d}L, \qquad (1)$$

where L denotes the maximum dimension of an ice crystal, D denotes the width that is perpendicular to the maximum dimension, and $n(L)$ is the ice crystal size distribution in terms of L. Equation (1) is consistent with the definition of EPS given in the VIIRS SRD, which states that the EPS is defined as "the ratio of the third moment of the droplet size distribution to the second moment, averaged over a layer of air within a cloud." To apply this definition to the ice crystal size distribution, we interpret that the third and second moments of the ice crystal size distribution to be the integration of the ice crystal size distribution weighted by the third and second power of a characteristic length (L or D) of an ice crystal, respectively.

To our knowledge, at this point there is limited information concerning the percentage distribution of ice crystal shapes for a given size distribution.[23] We propose to use ice crystal shape and associated aspect ratios on the basis of an *in situ* two-dimensional probe and replicator data. Following Takano and Liou,[21,22] we aggregated the size distributions into five bins: 10–30 μm with the bin center at 20 μm, 30–70 μm with the bin center at 50 μm, 70–170 μm with the bin center at 120 μm, 170–430 μm with the bin center at 300 μm, and 430–1070 μm with the bin center at 750 μm. The aspect ratios L/D, roughly corresponding to the observations reported by Auer and Veal,[24] are 20/20, 50/40, 120/60, 300/100, and 750/160 (in units of μm/μm) for each respective bin. The effective particle sizes for the above six reference ice crystal size distributions are (in the order of listing) 24, 30, 42, 75, 93, and 124 μm. It is well recognized that the EPS changes with height. However, the present retrieval algorithms produce vertically averaged EPSs, partly because satellite retrieval of the vertical distribution of ice crystal sizes within a cirrus cloud is still under development and is not mature enough to be incorporated into the VIIRS retrieval program. Ou *et al.*[16] used the FIRE-II data to show that retrieved mean effective ice crystal sizes differ from those derived from collocated balloon-borne replicator sonde measurements by less than 10 μm.

C. Single-Scattering Properties for Ice Crystals

In recent years, we developed a Monte Carlo geometric ray-tracing method for the computation of the scattering, absorption, and polarization properties of ice crystals with various structures.[25] The shape of these ice crystals is defined by appropriate geometric models and incident coordinate systems. The incident photons are traced with a hit-and-miss Monte

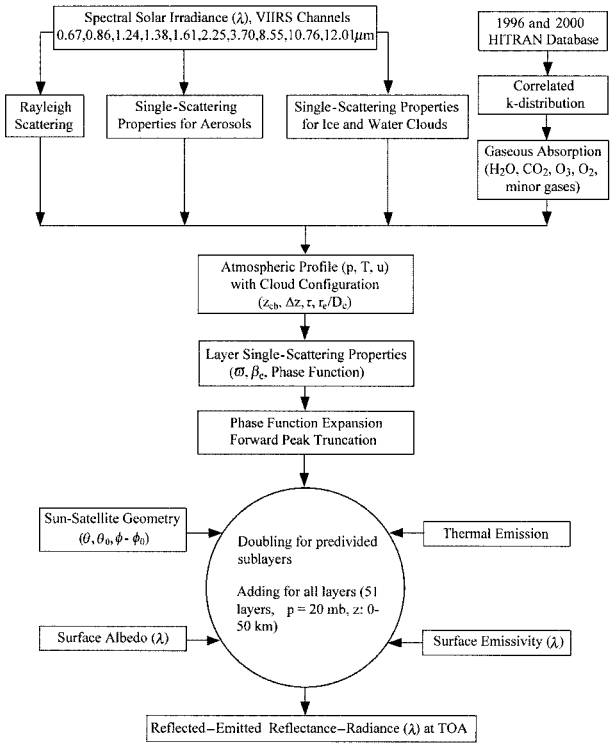

Fig. 2. Flow diagram of the LBLE radiative transfer program developed for the computation of top-of-the-atmosphere (TOA) radiance for the application to cloud remote sensing with VIIRS channels.

Carlo method and followed by geometric reflection and refraction on the crystal boundary. Absorption can be accounted for by means of stochastic procedures. In our calculations, we assume that ice crystals are randomly oriented hexagonal columns and plates. Comparisons of bidirectional reflectances obtained on the basis of this assumption with those from a scanning radiometer onboard NASA's ER-2 aircraft over Oklahoma on 24 and 25 November 1991 show that computed and measured values agree with each other reasonably well.[26] For some of the quasi-spherical ice particles, such as frozen droplets, we approximate them by spheroids. In those cases, the scattering and absorption properties can be computed by the anomalous diffraction theory combined with the geometric ray-tracing method.[27]

D. Radiative Transfer Model

With the radiative transfer model we use the adding–doubling method including full Stokes parameters developed by Takano and Liou[21,22] for vertically inhomogeneous atmospheres. The input parameters required to drive the LBLE solar radiation model include the solar insolation, spectral band wave numbers of interest, solar and viewing zenith angles, the relative azimuthal angle, spectral surface albedos and emissivities, atmospheric temperature and humidity, aerosol profiles, cloud phase, and cloud-top and base altitudes. Figure 2 shows the flow chart of the radiative transfer model developed for application to cloud remote sensing with VIIRS channel radiances. We first compile the spectral solar constant for VIIRS 0.67-, 0.86-, 1.24-, 1.38-, 1.61-, 2.25-, 3.70-, 8.55-, 10.76-, and 12.01-μm channels. With LBLE we can use the detailed solar irradiance data given by Thekaekara[28] (solar constant 1353 W/m^2), Kneizys *et al.*[29] (solar constant 1380 W/m^2), and Anderson *et al.*[30] (solar constant 1375 W/m^2) averaged over appropriate spectral resolutions. We then generate the gaseous absorption line parameters from the updated HITRAN-1996 database for the above VIIRS channels.

The correlated k coefficients for H_2O covering the spectral region from 2000 to 21,000 cm^{-1} (0.5–5 μm) are determined on the basis of the methodology developed by Fu and Liou,[31] in which efficient and accurate parameterizations for the calculation of the pressure- and temperature-dependent absorption coefficients are developed on the basis of theoretical values at three reference temperatures and 19 reference pressures. Absorption due to O_3 and O_2 bands is also included in the model based on Beer's law.[3] In addition, we compiled the single-scattering properties of six typical aerosol types provided in d'Almeida *et al.*[32] in connection with the LBLE model. In the present study we use the rural aerosol model with 23-km visibility at the surface, which is the same as the default aerosol model in MODTRAN. Input cloud configuration parameters include cloud base height (z_{cb}), cloud thickness (Δz), cloud optical depth (τ), and cloud EPS (r_e/D_e). At this point, the entire solar spectrum is divided into a total of 380 intervals, each of which is 50 cm^{-1} wide. For each spectral interval, the inverse of the cumulative probability function $k(g)$ is evaluated at 30 g values, where $0 < g < 1$. The resulting single-scattering parameters, cumulative k-distribution functions, and phase functions, as well as auxiliary data, were combined and built into the radiative transfer program.

We divide the model vertical domain into 51 layers ($\Delta p = 20$ mb for each layer except for the bottom layer, where $\Delta p = 13$ mb). The doubling procedures are applied to each layer, starting with an extremely thin layer with an optical depth $\sim 10^{-8}$, to obtain the layer reflection and transmission functions. Subsequently, the adding procedures are applied to the 51 layers to obtain the radiance at the top of atmosphere. For wavelengths between 3.5 and 5 μm, we take into account the thermal emission contributions in the solar flux transfer by adding the emission part $(1 - \varpi)\pi B_\nu(T)$ to the adding–doubling method in a manner described in Takano and Liou,[33] where ϖ is the single-scattering albedo and $B_\nu(T)$ is the Planck function for a given layer temperature T. The thermal emission part, although small, has not been accounted for previously in broadband solar flux calculations and could be a significant energy source in the upper part of the atmosphere.

We compared both clear and cloudy radiances from LBLE with those from MODTRAN.[19] Clear radiances differ by less than 10%, but cloudy radiances differ by more than 40% for an optical depth greater than 4.

These differences are possibly caused by the different treatment of multiple scattering in the two models.

E. Cirrus Cloud Retrieval Programs

Once a cirrus cloud pixel is identified, one of three retrieval programs is applied to the data associated with the pixel. The solar cloud retrieval scheme with the VIIRS 0.67-, 1.61-, and 2.25-μm reflectance is employed to infer daytime cirrus cloud optical depth and EPS. The IR cloud retrieval scheme with the VIIRS 3.70- and 10.76-μm radiance is employed to infer the nighttime cirrus cloud temperature, EPS, and optical depth. The daytime IR cloud retrieval scheme is also employed to infer daytime cirrus cloud temperature, EPS, and optical depth. However, the 3.70-μm radiance for local daytime contains a reflected solar radiation component, which needs to be removed.

A schematic description of the solar cirrus cloud retrieval algorithm is given as follows. The retrieval program follows the principle of the dual-solar-channel correlation technique.[6] We first prescribe the geometric parameters for each pixel, including the solar zenith angle, the radiometer viewing zenith angle, and the relative azimuthal angle. The surface albedo can be either obtained from the histogram of clear reflectances or determined on the basis of a climatological database of surface types[34,35] and spectral values of surface albedo for different surface types.[36] We then generate tables of reflectances for all combinations of reference EPS and optical depth and for all VIIRS cloud retrieval channels (0.67, 1.61, and 2.25 μm) using the LBLE radiative transfer program. A series of numerical iteration procedures of a least-squares fit[37] is set up to search for the computed reflectances that best match the measured reflectances. With this numerical scheme, we can minimize the sum of the square of the residual, which is defined as the difference between the natural logarithm of computed reflectance and the natural logarithm of the measured reflectance. The retrieved cloud parameters consist of the combination of optical depth and EPS that is associated with the best-fit reflectances, yielding the minimal residual. Further details of the retrieval scheme are given in Ou *et al.*[19]

With the IR cirrus cloud retrieval scheme, we use VIIRS 3.70- and 10.76-μm radiances to determine cirrus temperature and IR emissivities based on the principle of radiative transfer and parameterizations. The following set of nonlinear algebraic equations are solved numerically:

$$R_i = (1 - \epsilon_i)R_{ai} + \epsilon_i B_i(T_c) \qquad i = 1, 2, \tag{2}$$

$$B_1(T_c) = \sum_{n=0}^{3} a_n [B_2(T_c)]^n = f[B_2(T_c)], \tag{3}$$

$$\epsilon_i = 1 - \exp(-k_i \tau) \qquad i = 1, 2, \tag{4}$$

where R_{ai} denotes the upwelling radiance reaching the cloud base for the ith spectral band, T_c is the cirrus cloud-top temperature and ϵ_i is the emissivity, $B_i(T_c)$ are the Planck functions at T_c for the ith spectral band wavelength, and τ is the optical depth at $\lambda = 0.55$ μm. The first term on the right-hand side of Eq. (2) represents the contribution of the transmitted radiance from below the cloud. The second term denotes the emission contribution from the cloud itself. The emission by water vapor above the cirrus cloud was neglected. Further maneuver of Eqs. (2) and (4) yields

$$\frac{R_2 - B_2(T_c)}{R_{a2} - B_2(T_c)} = \left[\frac{R_1 - B_1(T_c)}{R_{a1} - B_1(T_c)}\right]^{\frac{k_2}{k_1}}. \tag{5}$$

In the algorithm development, we correlated ϵ_1 and ϵ_2 by introducing the ratio k_2/k_1, which is a function of the ice crystal size distribution. Using the six reference ice crystal size distributions described above, we developed a parameterization of k_2/k_1 in terms of the EPS:

$$k_2/k_1 = \sum_{n=0}^{2} b_n(\tau) D_e^{-n}. \tag{6}$$

To enhance the accuracy of Eq. (6), coefficients b_n are further expressed as a third-order polynomial function:

$$b_n(\tau) = \sum_{n=0}^{3} d_n \tau^n. \tag{7}$$

Moreover, to close the system of equations, an empirical relationship among D_e, τ, and T_c is derived based on the dimensional analysis[16]:

$$D_e = c\{\tau/[\Delta z(\alpha + \beta/D_e)\langle \mathrm{IWC}\rangle]\}^{1/3}\langle D_e\rangle, \tag{8}$$

where c is a proportional factor, Δz is the prescribed cloud thickness, IWC is the ice water content, $\langle D_e\rangle$ and $\langle$IWC$\rangle$ are the temperature-dependent mean values of the respective parameter,[3] and

$$\langle \mathrm{IWC}\rangle = \exp\{-7.6 + 4\exp[-0.2443 \times 10^{-3}(253 - T_c)^{-2.445}]\}, \tag{9}$$

$$\langle D_e\rangle = \sum_{n=0}^{3} c_n (T_c - 273)^n. \tag{10}$$

Equations (9) and (10) were derived for the midlatitude region. To apply these equations to the tropical region, the coefficients in Eqs. (9) and (10) need to be redefined based on *in situ* measurements.

Thus, Eqs. (2)–(4) and (6) and (8) form a complete set of seven governing equations for the solution of seven unknowns: ϵ_1, ϵ_2, $B_1(T_c)$, $B_2(T_c)$, T_c, τ, and D_e. Using the VIIRS 3.70- and 10.76-μm channel data, we first obtain an estimate of mean cirrus cloud temperature based on an optimization scheme.[18] Subsequently, an initial guess of ϵ_2, τ, k_2/k_1, and D_e can be determined based on the inverse form of Eqs. (2), (4), (6), and (8). We then proceed with the numerical iteration until the iterated value of T_c, τ, and D_e

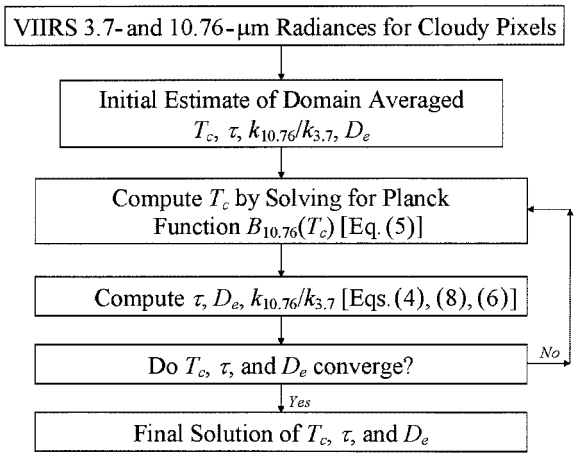

Fig. 3. Flow chart for the cirrus IR retrieval program.

converge. Figure 3 shows a flow chart for the above solution procedures.[19]

During daytime, the 3.70-μm radiance contains both thermal emission and solar reflection. To apply the preceding retrieval program, we developed an efficient but accurate scheme to remove the solar reflection part in the 3.70-μm radiance. This scheme is based on the correlation between 0.67- and 3.70-μm solar reflectances, which can be established based on the computations with the LBLE radiative transfer program. Effects of the possible sources of errors on the retrieval results have been carefully analyzed in previous studies based on synthetic retrieval analyses. Overall, the estimated maximum percentage error of the 3.70-μm solar component for removal is less than 10%.[15] The daytime retrieval scheme has also been applied to AVHRR data covering a 20° (latitude) by 30° (longitude) area over the Midwestern United States.[15]

3. Sensitivity Studies on the Retrieval of Cloud Optical Thickness and Effective Particle Size

To investigate the accuracy and precision of the retrieval method subject to instrument noise and uncertainties in environmental parameters, we carried out sensitivity studies on the retrieval of COT and EPS using the retrieval techniques described above for six artificial cirrus cloud scenes. These scenes are (1) nadir U.S. Standard Atmosphere over ocean, (2) off-nadir U.S. Standard Atmosphere over land, (3) edge-of-scan U.S. Standard Atmosphere over land, (4) nadir Tropical Atmosphere over land, (5) nadir Subarctic Atmosphere over snow and ice, and (6) nadir U.S. Standard Atmosphere over desert. The terms nadir, off nadir, and edge of scan denote the scan angle of the radiometer to be at 0°, 40°, and 56°, respectively. The LBLE was used to generate simulated radiance and reflectance for each scene. Input parameters specified for each scene include the atmospheric profile, geometry, retrieval channel characteristics (including central wavelength, bandwidth, and response function), cloud type, altitude and thickness, as well as surface albedo and emissivity. On basis of the VIIRS orbital information, the solar zenith angle θ_0 is 32° for scenes (1), (2), (3), and (6), corresponding to 1 May at 40 °N; θ_0 = 25.2° for scene (4), corresponding to tropical morning condition; and θ_0 = 42.4° for scene (5), corresponding to summer polar noontime condition. Over ocean, the surface albedo for all three solar channels is 0.05. Over land, the 0.67-μm surface albedo is 0.1, and the 1.61- and 2.25-μm surface albedo is 0.25. Over snow and ice, the 1.24- and 1.61-μm surface albedos are 0.16 and 0. Finally, over desert, the 0.67- and 1.61-μm surface albedos are 0.4 and 0.64, respectively. The radiative transfer calculations are performed for a wide range of selected optical depths and EPSs. For cirrus clouds, the optical depths chosen are 0.125, 0.25, 0.5, 1, 2, 3, 4, 5, 6, 7, 8, 9, 10, and 12. The EPSs chosen are those associated with the six analyzed size distributions. The single layer of cirrus cloud layer is fixed at 9–10 km for all scenes except scene (4). For scene (4), cirrus cloud is located at 14–15 km.

The SNR tests were carried out because the effects of SNR on pixel-level retrievals were a major concern during the early stage of instrument design. Retrievals are performed for a single pixel assuming various combinations of cloud optical depths and EPSs. Test results are presented separately for solar and IR methods. To create data sets to support the pixel-level SNR test, 32 sets of noises based on the sensor specification noise model are added directly to each entry in the LBLE-generated radiance–reflectance tables and then retrievals are performed with the noise-added data in the tables. Typical radiometric errors are approximately 2%. The results of the retrieval process are then statistically analyzed to compute the metrics described in the SRD[18] (accuracy and precision). The accuracy is defined as the absolute value of the mean retrieval errors:

$$\epsilon_a = |\epsilon| = \left| \frac{1}{N} \left[\sum_{i=1}^{N} (x_i - x_t) \right] \right|, \tag{11}$$

where ϵ_a is the accuracy, ϵ is the mean retrieval error, x_i is the retrieved EDR value based on the ith set of the perturbed radiance values, x_t is the true EDR value, and N is the total number of sets of the perturbed radiance values. The precision is similarly defined as

$$\epsilon_p = \left\{ \frac{1}{N} \left[\sum_{i=1}^{N} (x_i - x_t - \epsilon)^2 \right] \right\}^{1/2}. \tag{12}$$

A. Signal-to-Noise Ratio Tests: Solar Retrieval

SNR tests for the solar retrieval scheme were carried out for scenes (1)–(6), but only the results for scenes (1), (5), and (6) are shown here. Figure 4(a) shows the two-dimensional correlations for the unperturbed reflectance pairs, 0.67–1.61 and 0.67–2.25 μm for scene (1). Constant-value curves are plotted for the six ice crystal size distributions and for chosen optical depths. These diagrams clearly illustrate that the 0.67-, 1.61-, and 2.25-μm reflectances contain infor-

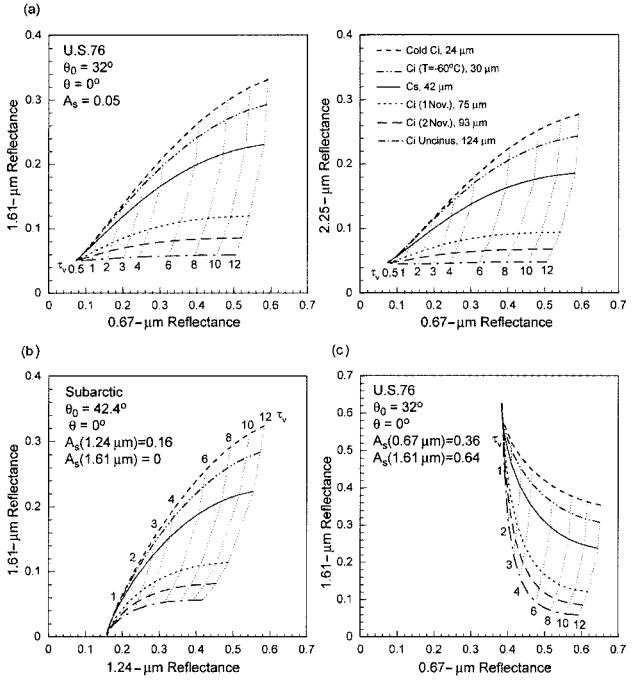

Fig. 4. (a) Display of the correlation between the VIIRS 0.67- and 1.61-μm reflectances and between the 0.67- and 2.25-μm reflectances for scene (1), nadir U.S. Standard Atmosphere (U.S. 76) over ocean; (b) display of the correlation between the VIIRS 1.24- and 1.61-μm reflectances for scene (5), nadir Subarctic Atmosphere over snow and ice; (c) display of the correlation between the VIIRS 0.67- and 1.61-μm reflectances for scene (6), nadir U.S. Standard Atmosphere (U.S. 76) over desert.

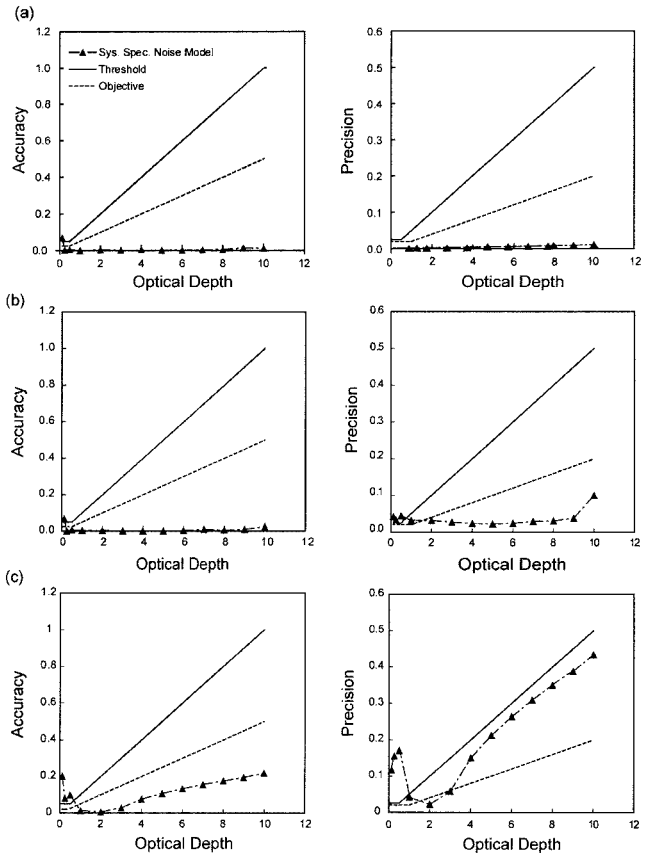

Fig. 5. Accuracy and precision errors of retrieved cloud optical depths from the SNR tests of the solar retrieval scheme as functions of optical depth for (a) scene (1), nadir U.S. Standard Atmosphere over ocean; (b) scene (5), nadir Subarctic Atmosphere over snow and ice; (c) scene (6), nadir U.S. Standard Atmosphere over desert. Sys. Spec., system specification.

mation of optical depth and EPS in the reflectances. The 0.67-μm reflectance mainly depends on the optical depth, whereas the 1.61- and 2.25-μm reflectances are primarily functions of EPS for optically thick ice clouds. Display of the 0.67- and 1.61-μm reflectance correlation indicates that if a data point falls within the correlation mesh, which is formed by curves of constant optical depth and constant EPS, then a meaningful retrieval of the two cloud EDRs can be achieved. Figure 4(b) shows the correlation between the 1.24- and 1.61-μm unperturbed reflectances for scene (5). The 1.24-μm reflectance is currently used in MODIS algorithms for the retrieval of cloud optical depth over ice and snow surfaces[38,39] because the 1.24-μm surface albedo over ice and snow surfaces is lower than that for 0.67 μm[40] and can be used to separate clouds from snow and ice surfaces. In the VIIRS solar retrieval technique, we replace the 0.67-μm reflectance with the 1.24-μm reflectance over snow and ice. Figure 4(c) shows the correlation between the 0.67- and 1.61-μm unperturbed reflectances for scene (6). Because the 0.67- and 1.61-μm surface albedos are higher than those over ocean and land, the reflectances shift to higher values and the sensitivity of the 0.67-μm reflectance to the optical depth is also reduced, as can be seen from the smaller differences in reflectances between constant optical depth curves.

Figures 5(a)–5(c) show the accuracy and precision of retrieved optical depths as functions of optical depth along with the threshold and objective requirements specified by the VIIRS SRD[18] for scenes (1), (5), and (6). We based these results on retrievals for combinations of all possible optical depths between 0.125 and 10 and EPSs between 24 and 124 μm using the correlations of the 0.67–1.61-μm reflectances for Figs. 5(a) and 5(c) and of the 1.24–1.61-μm reflectances for Fig. 5(b). For the purpose of reference, threshold and objective requirements in the form of two straight lines are included in the accuracy and precision diagrams. The accuracy errors of retrieved optical depths are smaller than both the threshold (greater of 10% or 0.05) and objective (greater of 5% or 0.025) requirements for optical depths larger than 0.5. The precision errors are also smaller than both the threshold (greater of 5% or 0.025) and the objective (greater of 2% or 0.02) requirements for the same range of optical depth. For optical depths less than 0.5, both the accuracy and the precision errors are close to the threshold and objective requirements. The extremely small values of accuracy and precision errors indicate that the solar retrieval scheme is highly accurate and numer-

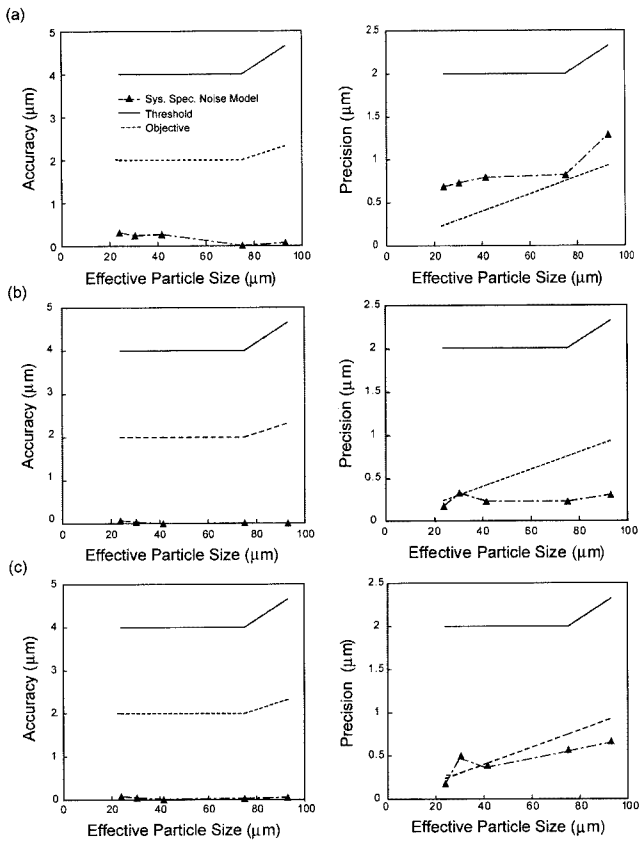

Fig. 6. Accuracy and precision errors of retrieved EPS from the SNR tests of the solar retrieval scheme as functions of EPS for (a) scene (1), nadir U.S. Standard Atmosphere over ocean; (b) scene (5), nadir Subarctic Atmosphere over snow and ice; (c) scene (6), nadir U.S. Standard Atmosphere over desert. Sys. Spec., system specification.

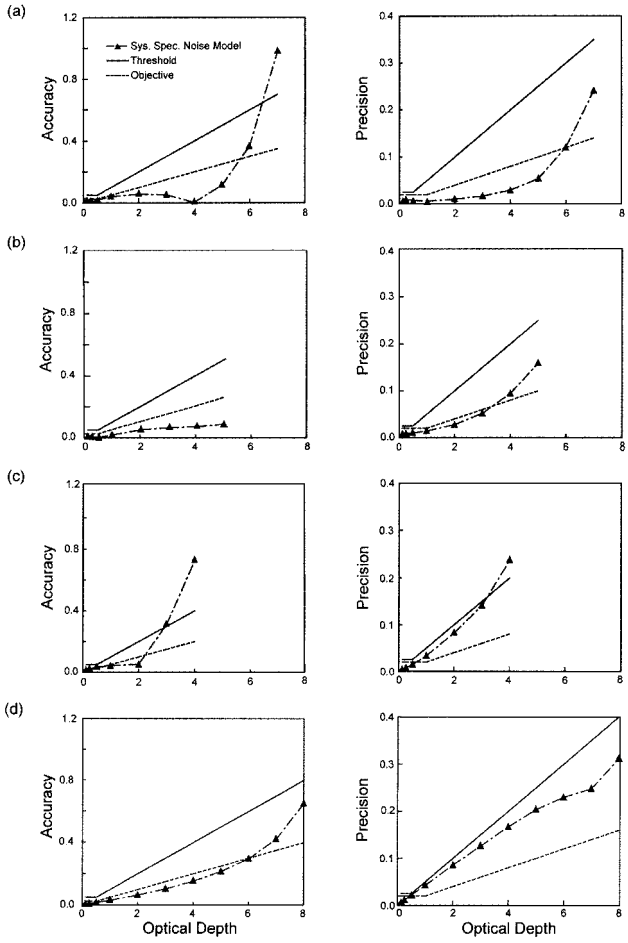

Fig. 7. Accuracy and precision errors of retrieved cloud optical depths from the SNR tests of the IR retrieval scheme as functions of optical depth for (a) scene (1), nadir U.S. Standard Atmosphere over ocean; (b) scene (2), off-nadir U.S. Standard Atmosphere over land; (c) scene (3), edge-of-scan U.S. Standard Atmosphere over land; (d) scene (4), nadir Tropical Atmosphere over land. Sys. Spec., system specification.

ically stable, if the error source is limited to the system-specified noise. Corresponding results for scenes (2)–(4) are similar to those shown in Fig. 4(a), indicating that, when the scanning direction of the radiometer or the atmospheric profile is varied, it has almost no effects on the retrieval accuracy and precision. The increase in accuracy and precision errors for the desert atmosphere [Fig. 5(c)] is due to the reduced sensitivity of 0.67-μm reflectance to the optical depth. When the 1.61-μm reflectance is replaced with the 2.25-μm reflectance in the retrieval of COT, the accuracy and precision errors still satisfy both the threshold and the objective requirements. Thus we expect that the retrievals with the 0.67–2.25-μm correlations will produce similar results as those with the 0.67–1.61-μm correlations. For the rest of the algorithm studies on the solar retrieval algorithm, only results based on the 0.67–1.61-μm correlation are shown.

Figures 6(a)–6(c) show the accuracy and precision of retrieved EPSs as functions of EPS. The two straight lines denote threshold and objective requirements. We divide errors in D_e by two to yield errors in effective radius for ice clouds as required by the SRD. The accuracy errors satisfy both the threshold (greater of 10% or 4 μm) and the objective (greater of 5% or 2 μm) requirements for the full range of specified EPSs and are approximately the same magnitude across the size range. The precision errors meet the threshold (greater of 5% or 2 μm) requirement for the full size range. The small accuracy and precision errors indicate that the solar retrieval scheme is both accurate and numerically stable when we retrieve EPSs subject to system specification radiometer noises. In general, precision errors increase with increasing EPS because of the reduction of the sensitivity of the 1.61-μm reflectance to the EPSs as evidenced by the closeness of constant-size curves for larger EPS (Fig. 4).

B. Signal-to-Noise Ratio Tests: IR Retrieval

SNR tests for the IR retrieval scheme were carried out for scenes (1)–(4). Figures 7(a)–7(d) show the accuracy and precision errors of retrieved cloud optical depth from the IR retrieval scheme as a function of cloud optical depth for scenes (1)–(4), respectively.

Two straight lines denote threshold and objective requirements, which are the same as depicted in Fig. 5. For scenes (1)–(3), both accuracy and precision errors satisfy the threshold requirement for optical depths 0–6, 0–5, and 0–3, respectively. For optical depths larger than these limiting values, the accuracy and precision errors exceed the threshold value. According to Eq. (4), the IR emissivity of optically thick clouds approaches 1 as the clouds are becoming thermally black, and the sensitivity of the emitted radiance to the optical depth is drastically reduced. Therefore a small error in the measured radiance over a pixel that contains optically thick cloud can lead to a large uncertainty in retrieved optical depth. This is a unique characteristic of the IR cloud retrieval scheme. For the tropical scene (4), both accuracy and precision errors satisfy the threshold requirement for optical depths 0–8. In particular, in contrast to Fig. 7(a), these errors still satisfy the threshold requirement for optical depths 6–8. Because the difference between cloud-top and surface temperatures for the tropical atmosphere (96 K) is larger than that for the mid-latitude atmosphere (64 K), the sensitivity of the emitted radiance to the optical depth is larger, leading to smaller errors near the black-cloud limit.

Figures 8(a)–8(d) show the accuracy and precision of retrieved EPSs from the IR retrieval scheme as a function of optical depth for scenes (1)–(4), respectively. These results are based on retrievals of combinations of optical depths between 0.125 and 7 for the EPS fixed at 42 μm. The two horizontal straight lines denote threshold and objective requirements. For scenes (1)–(3), the accuracy errors satisfy the threshold requirement (4 μm) for optical depths 0–5, 0–4, and 1–3, and the precision errors satisfy the threshold requirement (2 μm) for optical depths 1–5, 1–5, and 1–4, respectively. The accuracy errors exceed the threshold for larger optical depths, mainly because of the indirect effects of the reduced sensitivity of the emitted radiance to the optical depth for optically thick clouds. As the emissivity approaches unity, small errors in the measured radiance will be amplified in the retrieved optical depth because of the reduced sensitivity, and thus the accuracy of the retrieved EPS, which depends on the accuracy of the retrieved optical depth, is also affected. On the other hand, precision errors exceed the threshold for optical depths smaller than 1. This is because, as the emissivity approaches zero, errors in the retrieved cloud-top temperature increase. Therefore the accuracy of the retrieved EPS, which depends on the accuracy of the retrieved cloud temperature, becomes worse for smaller optical depths. Moreover, the range of optical depths for which the threshold and objective requirements are met becomes smaller for larger ice crystal EPS (not shown) because, as the EPS increases, the sensitivity of the 3.70-μm radiance to the EPS decreases. For the tropical scene (4), accuracy errors satisfy the objective requirement for optical depths 0.5–6, and precision errors satisfy the threshold requirement for optical depths 1–6.

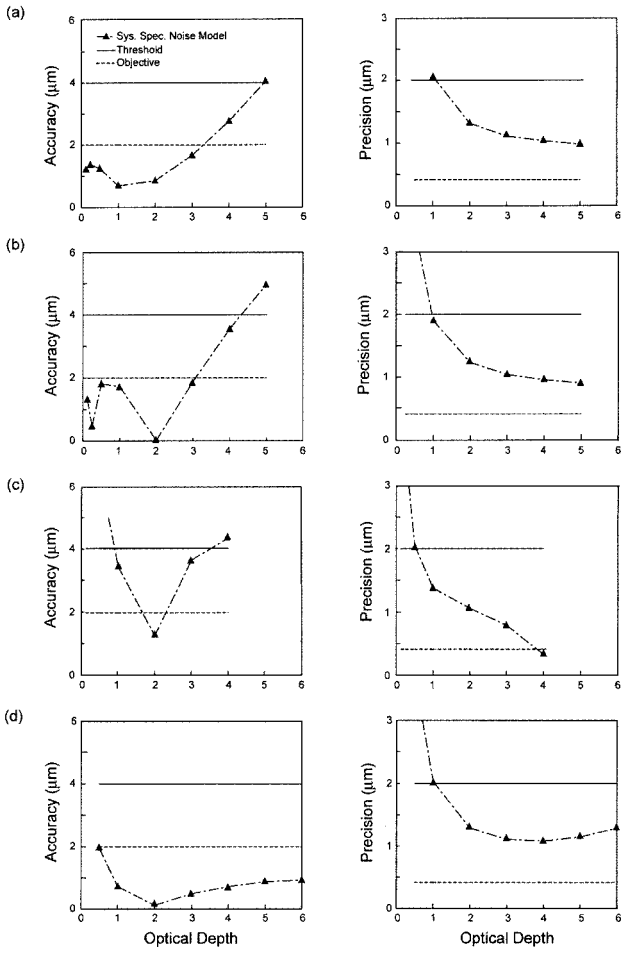

Fig. 8. Accuracy and precision errors of retrieved EPS from the SNR tests of the IR retrieval scheme as functions of optical depth with the true EPS fixed at 42 μm for (a) scene (1), nadir U.S. Standard Atmosphere over ocean; (b) scene (2), off-nadir U.S. Standard Atmosphere over land; (c) scene (3), edge-of-scan U.S. Standard Atmosphere over land; (d) scene (4), nadir Tropical Atmosphere over land. Sys. Spec., system specification.

The higher retrieval accuracy and precision are due to the larger sensitivity of the 3.7-μm radiance to the particle size caused by the larger temperature difference between the surface and the cloud top.

C. Error Budget Studies

We have attempted to quantify the effects of a number of error sources in input parameters and in sensor-measured radiances on the performance of cloud algorithms. For input parameter errors, our approach has been to develop partial derivatives that quantify the change in measurement accuracy or precision metric value to a small perturbation in a single input parameter. These partial derivatives are then multiplied by a standard error, which captures the anticipated root-mean-square error in that input parameter. The product of the partial derivative with the standard error gives an estimate of the input parameter's contribution to the error budget for a given EDR.

The standard error for surface albedo or surface

emissivity is prescribed to be 0.01, given that the surface considered for the three viewing angles is ocean and that the surface albedo over ocean is relatively uniform (~0.05). The standard errors for the surface temperature and the vertical temperature, relative humidity, and pressure profiles are 1 K, 1 K, 20%, and 10 mb, respectively. Although uncertainties in radiosonde temperatures at approximately 0.5 K have been noted, somewhat larger prescribed errors of 1 K seem appropriate for profiles derived from a combination of analyses of soundings and forecasts from numerical weather prediction models. Prescribed errors of 20% for the input relative humidity profile are typical uncertainties for soundings. Perturbations due to input parameters are determined by the reevaluation of the radiance and reflectance from the radiance tables.

The error sources for sensor-measured radiances include system-specified noise, band-to-band registration errors (0.2 pixel shift), errors in the modulated transmission function, geolocation (0.2 pixel shift), and absolute radiometric calibration (2% for solar channels; 0.4% for IR channels). A Gaussian distribution is used to simulate perturbation to radiances.

Error budgets have been developed by the application of the retrieval schemes to defined cloudy domains, covering approximately a 100 km × 100 km area. The spatial distribution of cloud properties within the area is determined by use of the Northrop Grumman TASC's Cloud Scene Simulation Model (CSSM). The processing of CSSM data yields a horizontal distribution of cloud optical depth at 0.1-km spatial resolution for a layer of cloud with D_e = 42 μm. The prescribed geometry, surface characteristics, atmospheric profiles, and cloud-top and base heights of scenes (1), (2), and (3) are used to develop radiance and reflectance tables for VIIRS cloud retrieval channels as functions of cloud EPS and optical depth. We use these radiance–reflectance tables to create images for each channel by assigning a value from the tables to the optical depth associated with each 0.1-km data point. The 0.1-km data are aggregated to the VIIRS pixel size.

The unperturbed and perturbed radiances are used to produce truth and noisy retrieval results at the pixel level, respectively. Then we obtain accuracy and precision error metrics for a horizontal cell size (HCS) of 25 km, based on Eqs. (11) and (12). For sensor error sources, these are the metrics required by SRD. However, for input parameter errors, we first divide the metrics by the small perturbation to compute the partial derivatives, and then we multiply the partial derivatives with the standard errors to obtain the metrics required by SRD. Finally, we determine the total error budget as the root-mean-square sum of the individual error metrics.

Figures 9(a) and 9(b) show error budget bar charts for the accuracy and precision errors of retrieved cirrus cloud optical depths for solar and IR retrieval schemes based on the input parameters of scene (1), respectively. These error statistics are presented in terms of four optical depth bins (0.5–1, 1–5, 5–10, and 0–10) and a weighted average bin. These optical depths correspond to the cloud optical depth distribution in the CSSM. The errors for the weighted average bin are generated on the basis of the sum of errors for the first three bins weighted by the sample population of each bin. Figure 9(a) shows that, for all except the (0.5–1) bins, the solar retrieval scheme produces accuracy and precision errors that are lower than threshold and objective requirements for nadir, off-nadir, and edge-of-scan cases. These error budget estimates are larger than those shown in Fig. 5(a) because, in addition to the system specification errors, additional uncertainties due to various standard error sources were added to the input reflectances. Figure 9(b) shows that the error budget for the IR retrieval of cloud optical depths is less satisfactory. For the nadir case, the accuracy and precision errors satisfy threshold requirements for all bins except bin (0.5–1). For the off-nadir case, the accuracy errors satisfy threshold requirements for bin (1–5), but the precision errors satisfy threshold requirements for all bins. For the edge-of-scan case, threshold limits are exceeded by both accuracy and precision errors for all bins. These large errors are expected because the edge-of-scan case is the most difficult in terms of satisfying threshold requirements.

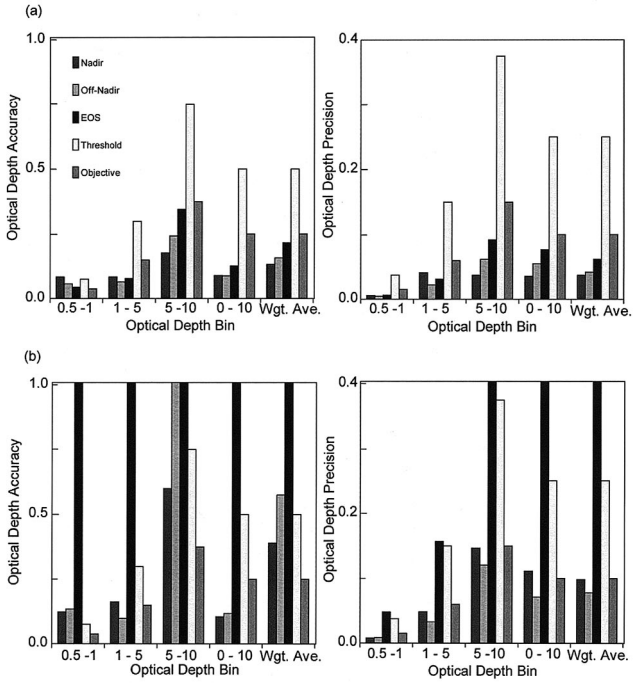

Fig. 9. Bar charts of accuracy and precision errors of retrieved cloud optical depths from the error budget study of (a) the solar retrieval scheme and (b) the IR retrieval scheme based on the CSSM-generated distribution of cloud optical depth and input parameters of scene (1), nadir U.S. Standard Atmosphere. Wgt. Ave., weighted average.

Figures 10(a) and 10(b) show error budget bar charts for the retrieval errors of cirrus cloud EPS for solar and IR retrieval schemes based on the input parameters of scene (1), respectively. Figure 10(a)

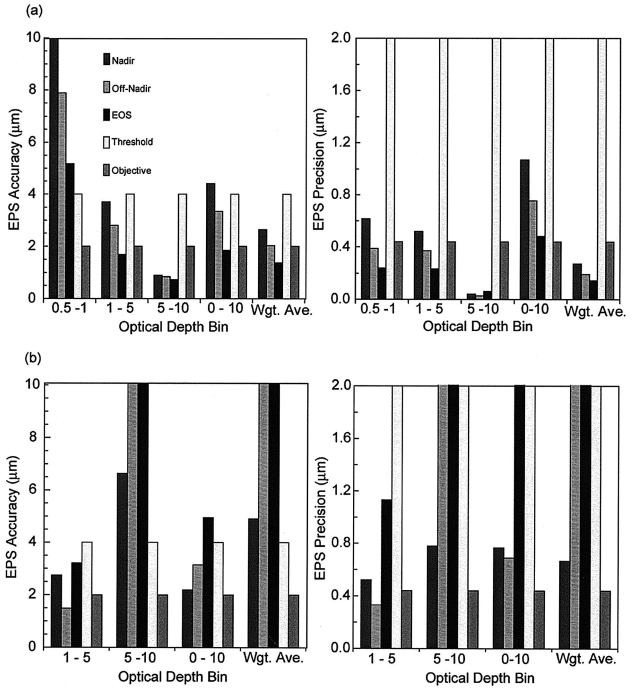

Fig. 10. Bar charts of accuracy and precision errors of retrieved EPS from the error budget study of (a) the solar retrieval scheme and (b) the IR retrieval scheme based on the CSSM-generated distribution of cloud optical depth and input parameters of scene (1), nadir U.S. Standard Atmosphere. Wgt. Ave., weighted average; EOS, Earth Observing System.

shows that, except for bins (0.5–1) and (0–10), the accuracy errors for the nadir case satisfy the threshold requirement and, in some cases, satisfy the objective requirement. The precision errors for the nadir case satisfy the threshold requirement for all bins. Except for bin (5–10), the accuracy errors for the off-nadir case satisfy the threshold requirement. The precision errors for the off-nadir case satisfy the threshold requirement for all bins. Errors for the edge-of-scan case satisfy both threshold and objective requirements for all bins except bin (0.5–1). We note that the accuracy and precision errors actually are smaller for the edge-of-scan case than for the nadir and off-nadir cases because of the enhanced absorption effect due to longer absorption path lengths. Figure 10(b) shows that, for bins (1–5) and (0–10), accuracy and precision errors satisfy the threshold requirement for nadir and off-nadir cases, and that for the edge-of-scan case, accuracy and precision errors satisfy the threshold requirement only for bin (1–5), as expected. Overall, the retrieval of cirrus cloud EPS with both solar and IR techniques satisfies VIIRS SRD requirements for radiometer scanning angles less than 40°.

4. Summary

To assist the design of the NPOESS VIIRS radiometer, we have developed retrieval schemes for inferring cirrus cloud optical depth and EPS. The solar retrieval scheme uses the reflectance of VIIRS 0.67-, 1.24-, 1.61-, and 2.25-μm channels and follows the two-channel correlation technique to retrieve the cirrus cloud optical depth and EPS during daytime. The IR approach utilizes the radiance of VIIRS 3.70- and 10.76-μm channels and follows the two-channel cirrus technique to infer the cloud-top temperature and IR emissivity during nighttime. Application of the IR approach during the local daytime requires the removal of the solar component in the 3.70-μm radiance. The cloud optical depth and EPS can then be determined on the basis of the theory and parameterizations of radiative transfer and cloud microphysics. Although initial success has been achieved for the retrieval of cloud optical and microphysical parameters with both solar and IR approaches that were applied to surrogate satellite and airborne data, further algorithm sensitivity and validation studies are required to assess the accuracy and precision of these methods when applied to global cirrus cloud mapping with the VIIRS instrument.

To investigate the accuracy and precision of the retrieval methods subject to instrument noise and uncertainties in environmental parameters, we carried out a series of SNR tests and error budget analyses. We use the LBLE radiative transfer model developed at UCLA to generate radiance tables for various combinations of cloud optical depths and EPSs. For this purpose, we have analyzed six composite ice crystal size distributions that were obtained from aircraft observations over mid-latitude regions and have computed the single-scattering properties associated with these size distributions. We have defined six artificial cirrus cloud scenes with different atmospheric profiles, cirrus cloud properties and heights, surface types, and varying radiometric scanning angles.

For the SNR tests, we used the UCLA LBLE-generated radiance tables covering a measurement range of both cloud optical depth and EPS. Randomly distributed noises are added to these radiances according to the system specification noise model. These simulated radiances are then applied to retrieval algorithms. For error budget studies, perturbations of the no-noise radiance tables for various error sources were carried out to simulate typical uncertainties in sensor parameters, surface characteristics, and atmospheric soundings. Using the CSSM along with the perturbed radiance tables, we generated cloud optical depth and associated reflectance–radiance fields for several defined scenes. We developed error budgets by applying these reflectance–radiance fields to retrieval algorithms.

We have demonstrated that the UCLA LBLE radiative transfer program has the capacity to compute simulated NPOESS VIIRS cloudy reflectance and radiance for all combinations of selected values of cloud optical depth and EPS and for different atmospheric scenes. We have also shown that accuracy and precision errors from the solar and IR retrieval schemes satisfy NPOESS VIIRS design requirements for most optical depths and EPSs and for different atmospheric conditions. In the future, we would like to

develop multilayer cloud retrieval schemes and investigate their accuracy in a similar manner as in this paper. We would also like to apply the solar and IR retrieval schemes to recently available surrogate satellite (MODIS onboard Terra or Aqua) and airborne (MODIS Airborne Simulator) radiometric data collected during field campaigns and over permanent field observation sites. We will investigate the sensitivity to the variation in EPS and cloud-top and base pressures, shadowing, and other three-dimensional effects.

This research was supported by Raytheon ITSS Corporation contract 4500008484 through the NPOESS Integrated Program Office.

References

1. M. D. King, S.-C. Tsay, S. E. Platnick, M. Wang, and K. N. Liou, "Cloud retrieval algorithms for MODIS: optical thickness, effective particle radius, and thermodynamic phase," MODIS Algorithm Theoretical Basis Document ATBD-MOD-05 (NASA Goddard Space Flight Center, Greenbelt, Md., 1996), available at http://modis-atmos.gsfc.nasa.gov/_docs/atbd_mod05.pdf.
2. P. Minnis, D. F. Young, D. P. Kratz, J. A. Coakley, Jr., M. D. King, D. P. Garber, P. W. Heck, S. Mayor, and R. F. Arduini, "Clouds and the Earth's Radiant Energy System (CERES) Algorithm Theoretical Basis Document, Cloud Optical Property Retrieval," CERES ATBD Subsystem 4.3 (NASA Langley Research Center, Hampton, Va., 1997), available at http://eospso.gsfc.nasa.gov/eos_homepage/for_scientists/atbd/docs/CERES/atbd-cer-08.pdf.
3. K. N. Liou, *An Introduction to Atmospheric Radiation*, 2nd ed. (Academic, Amsterdam, The Netherlands, 2002).
4. J. E. Hansen and J. B. Pollack, "Near-infrared light scattering by terrestrial clouds," J. Atmos. Sci. **27,** 265–281 (1970).
5. S. Twomey and T. Cocks, "Spectral reflectance of clouds in the near-infrared: comparison of measurements and calculations," J. Meteorol. Soc. Jpn. **60,** 583–592 (1982).
6. T. Nakajima and M. D. King, "Determination of the optical thickness and effective particle radius of clouds from reflected solar radiation measurements. Part I: Theory," J. Atmos. Sci. **47,** 1878–1893 (1990).
7. M. D. King, Y. J. Kaufman, W. P. Menzel, and D. Tanre, "Remote sensing of cloud, aerosol, and water vapor properties from the Moderate Resolution Imaging Spectrometer (MODIS)," IEEE Trans. Geosci. Remote Sens. **30,** 2–27 (1992).
8. B. A. Baum, D. P. Kratz, P. Yang, S. C. Ou, Y. Hu, P. Soulen, and S. C. Tsay, "Remote sensing of cloud properties using MODIS airborne simulator imagery during SUCCESS. I. Data and models," J. Geophys. Res. **105,** 11767–11780 (2000).
9. P. Rolland, K. N. Liou, M. D. King, S. C. Tsay, and G. M. McFarquhar, "Remote sensing of optical and microphysical properties of cirrus clouds using MODIS channels: methodology and sensitivity to physical assumptions," J. Geophys. Res. **105,** 11721–11738 (2000).
10. P. Rolland and K. N. Liou, "Surface variability effects on the remote sensing of thin cirrus optical and microphysical properties," J. Geophys. Res. **106,** 22965–22977 (2001).
11. G. Szejwach, "Determination of semi-transparent cirrus cloud temperature from infrared radiances: application to METEOSAT," J. Appl. Meteorol. **21,** 384–393 (1982).
12. A. Arking and J. D. Childs, "Retrieval of cloud cover parameter from multi-spectral satellite images," J. Clim. Appl. Meteorol. **23,** 322–333 (1985).
13. K. N. Liou, S. C. Ou, Y. Takano, F. P. J. Valero, and T. P. Ackerman, "Remote sounding of the tropical cirrus cloud temperature and optical depth using 6.5 and 10.5 μm radiometers during STEP," J. Appl. Meteorol. **29,** 715–726 (1990).
14. S. C. Ou, K. N. Liou, W. M. Gooch, and Y. Takano, "Remote sensing of cirrus cloud parameters using advanced very-high-resolution radiometer 3.7- and 10.9-μm channels," Appl. Opt. **32,** 2171–2180 (1993).
15. N. X. Rao, S. C. Ou, and K. N. Liou, "Removal of the solar component in AVHRR 3.7-μm radiances for the retrieval of cirrus cloud parameters," J. Appl. Meteorol. **34,** 481–499 (1995).
16. S. C. Ou, K. N. Liou, Y. Takano, N. X. Rao, Q. Fu, A. J. Heymsfield, L. M. Miloshevich, B. Baum, and S. A. Kinne, "Remote sounding of cirrus cloud optical depths and ice crystal sizes from AVHRR data: verification using FIRE-II-IFO composite measurements," J. Atmos. Sci. **52,** 4143–4158 (1995).
17. S. C. Ou, K. N. Liou, and T. R. Caudill, "Remote sounding of multilayer cirrus cloud systems using AVHRR data collected during FIRE II IFO," J. Appl. Meteorol. **37,** 241–254 (1998).
18. Associate Directorate for Acquisition NPOESS Integrated Program Office, "Visible/Infrared Imager/Radiometer Suite (VIIRS) Sensor Requirements Document (SRD) for National Polar-Orbiting Operational Environmental Satellite System (NPOESS) spacecraft and sensors," Version 2, Rev. a (National Polar-Orbiting Operational Environmental Satellite System Integrated Program Office, Silver Spring, Md., 2000).
19. S. C. Ou, K. N. Liou, Y. Takano, G. J. Higgins, A. George, and R. Slonaker, "VIIRS cloud effective particle size and cloud optical depth algorithm theoretical basis document," Algorithm Theoretical Basis Document, Version 5, Rev. 1 (Raytheon, Lanham, Md., 2002).
20. A. J. Heymsfield and C. M. R. Platt, "A parameterization of the particle size spectrum of ice clouds in terms of the ambient temperature and ice water content," J. Atmos. Sci. **41,** 846–855 (1984).
21. Y. Takano and K. N. Liou, "Solar radiative transfer in cirrus clouds. I. Single-scattering and optical properties of hexagonal ice crystals," J. Atmos. Sci. **46,** 3–19 (1989).
22. Y. Takano and K. N. Liou, "Solar radiative transfer in cirrus clouds. II. Theory and computation of multiple scattering in an anisotropic medium," J. Atmos. Sci. **46,** 20–36 (1998).
23. A. J. Heymsfield, A. Bansemer, S. Lewis, J. Iaquinta, M. Kajikawa, C. Twohy, and M. Poellot, "A general approach for deriving the properties of cirrus and stratiform ice cloud particles," J. Atmos. Sci. **59,** 3–29 (2002).
24. A. H. Auer, Jr. and D. L. Veal, "The dimension of ice crystals in natural clouds," J. Atmos. Sci. **27,** 919–926 (1970).
25. Y. Takano and K. N. Liou, "Radiative transfer in cirrus clouds. Part III: Light scattering by irregular ice crystals," J. Atmos. Sci. **52,** 818–837 (1995).
26. K. N. Liou, Y. Takano, and P. Yang, "Light scattering and radiative transfer in ice crystal clouds: applications to climate research," in *Light Scattering by Nonspherical Particles*, M. I. Mischenko, J. W. Hovenier, and L. D. Travis, eds. (Academic, New York, 2000), pp. 417–449.
27. Y. Takano, K. N. Liou, and P. Minnis, "Effects of small ice crystals on cirrus infrared radiative properties," J. Atmos. Sci. **49,** 1487–1493 (1992).
28. M. P. Thekaekara, "Solar irradiance: total and spectral and its possible variation," Appl. Opt. **15,** 915–920 (1976).
29. F. X. Kneizys, E. P. Shettle, L. W. Abreu, J. H. Chetwynd, G. P. Anderson, W. O. Gallery, J. E. A. Selby, and S. A. Clough, "User's guide to LOWTRAN 7" (U.S. Air Force Geophysics Laboratory, Hanscom Air Force Base, Mass., 1988).
30. G. P. Anderson, R. H. Picard, and J. H. Chetwynd, eds., *Proceedings of the 17th Annual Review Conference on Atmospheric Transmission Models*, Special Rep. 274 (Phillips Laboratory/Geophysics Directorate, Hanscom Air Force Base, Mass., 1995).
31. Q. Fu and K. N. Liou, "On the correlated *k*-distribution method

for radiative transfer in nonhomogeneous atmospheres," J. Atmos. Sci. **49,** 2139–2156 (1992).
32. G. A. d'Almeida, P. Koepke, and E. P. Shettle, *Atmospheric Aerosols, Global Climatology and Radiative Characteristics* (Deepak, Hampton, Va., 1991).
33. Y. Takano and K. N. Liou, "Transfer of polarized infrared radiation in optically anisotropic media: application to horizontally oriented ice crystals," J. Opt. Soc. Am. A **10,** 1243–1256 (1993).
34. T. R. Loveland, J. W. Merchant, J. F. Brown, D. O. Ohlen, B. C. Reed, P. Olson, and J. Hutchinson, "Seasonal land-cover of the United States," Ann. Assoc. Am. Geogr. **85,** 339–355 (1995).
35. A. Strahler, D. Muchnoney, J. Borak, M. Friedl, S. Gopal, E. Lambin, and A. Moody, "MODIS land cover and land-cover change," MODIS Land Cover Product Algorithm Theoretical Basis Document, (Boston University, Boston, Mass., 1999), available at http://modis.gsfc.nasa.gov/data/atbd/atbd_mod12.pdf.
36. CERES/SARB Surface Properties, available at http://www-surf.larc.nasa.gov/surf/pages/explan.html.
37. S. Twomey and T. Cocks, "Remote sensing of cloud parameters from spectral reflectance in the near-infrared," Beitr. Phys. Atmos. **62,** 172–179 (1989).
38. S. Platnick, J. Y. Li, M. D. King, H. Gerber, and P. V. Hobbs, "A solar reflectance method for retrieving the optical thickness and droplet size of liquid water clouds over snow and ice surfaces," J. Geophys. Res. **106,** 15185–15199.
39. S. Platnick, M. D. King, S. A. Ackerman, W. P. Menzel, B. A. Baum, and R. A. Frey, "The MODIS cloud products: algorithms and examples from Terra," IEEE Trans. Geosci. Remote Sens. **41,** 459–473 (2003).
40. G. T. Arnold, S. C. Tsay, M. D. King, J. Y. Li, and P. F. Soulen, "Airborne spectral measurements of surface-atmosphere anisotropy for arctic sea ice and tundra," Int. J. Remote Sens. **23,** 3763–3781 (2002).